High Voltage

Special Issue: The State-of-the-Art Research on Low Temperature Plasma

IET Journals
The Institution of Engineering and Technology

Comparison between electropositive and electronegative cold atmospheric-pressure plasmas: a modelling study

ISSN 2397-7264
Received on 18th May 2016
Revised on 4th June 2016
Accepted on 4th June 2016
doi: 10.1049/hve.2016.0019
www.ietdl.org

Ding Xin Liu[1], Jia Feng Li[1], Ai Jun Yang[1], Xiao Hua Wang[1] ✉, Ming Zhe Rong[1], Michael G. Kong[1,2,3]

[1]*State Key Laboratory of Electrical Insulation and Power Equipment, Centre for Plasma Biomedicine, Xi'an Jiaotong University, Shaanxi 710049, People's Republic of China*
[2]*Frank Reidy Center for Bioelectrics, Department of Electrical & Computer Engineering, Old Dominion University, Virginia 23508, USA*
[3]*Department of Electrical and Computer Engineering, Old Dominion University, Virginia 23529, USA*
✉ *E-mail: xhw@mail.xjtu.edu.cn*

Abstract: Cold atmospheric-pressure $He + N_2$ and $He + O_2$ plasmas are chosen as the representatives for electropositive and electronegative plasmas, of which the discharge characteristics are studied and then compared to each other by fluid models. As the increase of the impurity (N_2 or O_2) fraction from 0 to 10%, for $He + N_2$ plasmas the electron density and ion density increase, the spatiotemporal distributions of electron density, ion density, electron temperature and electron generation rate change a little. On contrast, for $He + O_2$ plasmas the electron density decreases, the ion density first increases and then decreases, the electron temperature increases in the bulk region, but decreases in the sheath region, and the plasmas transform from γ mode to α mode as the significant change of electron generation rate distributions. Larger electric field is needed in the bulk region to sustain the electronegative plasma, so the electrical characteristics of $He + O_2$ plasmas transform form capacitive to resistive with increasing O_2 fraction. Meanwhile, the ion-coupling power increases dramatically, which can be estimated by a formula based on the electronegativity. A new criterion for determining the sheath boundary, $|\nabla E| = 5$ kV/cm^2, is put forward, which is found suitable for both the electropositive and electronegative plasmas.

1 Introduction

Cold atmospheric-pressure plasmas (CAPs) have great application prospects in the fields of environmental protection [1], biomedicine [2], nano-technology [3] and so on. Most CAPs are operated in a noble gas, but with a small amount of molecular gases such as N_2 and O_2 [4]. The molecular gases are sometimes artificially mixed into the noble gas to make the plasmas more reactive and hence beneficial for various applications. For example, the typically small fraction between 0.5 and 3% of O_2 is added into helium to optimise the production efficiency of reactive oxygen species [5]. On the other hand, the molecular gases are inevitably existed due to the impurity of industrial noble gases, as well as the inclusion of air when the plasmas are not well sealed [6–10]. The electropositive nature of noble gases allows the plasmas to be sustained in relatively low electric field, which is one of the main reasons that keeping the plasmas cold, diffusive and stable [11]. However, the molecular gases such as O_2 and H_2O are strongly electronegative, and hence inhibit the plasma generation by absorbing the electrons. The plasma characteristics such as the volt-ampere characteristics can be changed significantly even when the fraction of electronegative gas is as low as 0.1% [4]. The electropositive CAPs and their electronegative counterparts have much different characteristics, which have not yet been well understood. This motivates us to compare the characteristics of those plasmas in quantitative level.

In this paper, $He + N_2$ and $He + O_2$ CAPs are chosen as the representatives of the electropositive and electronegative plasmas, respectively. The impurity (N_2 or O_2) fraction in the working gas is varied from 0 to 10%, covering most cases of practical applications. The electronegativity of $He + O_2$ CAPs keeps increasing with the O_2 fraction, allowing the plasma characteristics to be studying for a large electronegative range. A fluid model is used for this study, which has been used for $He + N_2$ and $He + O_2$ CAPs as reported previously [12–16]. The spatiotemporal evolution of the electron density, the electron temperature, the electron generation rate as well as the dissipated power density is obtained as a function of the impurity fraction, and they are compared with respect to the electropositive and electronegative plasmas. Moreover, the sheath dynamics is found to be much different for the two kinds of plasmas, and a new criterion is suggested for determining the sheath edge for those plasmas.

The paper is organised as follows: the computation model is described in Section 2, the simulation results are presented and discussed in Section 3, and at last conclusions are given in Section 4.

2 Description of the computational model

The discharge considered in this study is generated between two circular electrodes with a narrow separation of 0.2 cm and a large electrode width [to facilitate the use of one-dimensional (1D) model], similar to those used in experimental study [17]. One electrode is connected to a sinusoidal voltage with radio frequency of $f = 13.56$ MHz, the other one is grounded. The dissipated power density is kept constant to be 40 W/cm^3. For the purpose of comparing the $He + N_2$ and $He + O_2$ CAPs, all the discharge conditions are kept the same, and the impurity (N_2 or O_2) fraction is varied from 0 to 10%.

1D fluid models are used for $He + N_2$ and $He + O_2$ CAPs with their details previously reported [12–16] so just briefly described here. Nine species and 18 chemical reactions are incorporated for $He + N_2$ plasmas, while 17 species and 60 chemical reactions are incorporated for $He + O_2$ plasmas. The plasma chemistry used in this study is recommended by the authors [6, 13], and the plasma species are listed in Table 1.

The fluid models solve the mass conservation equation for each species (1), the Poisson's equation (2), and the electron energy conservation equation (3). Given the high collisionality of the discharge, the particles inertia is neglected and the drift-diffusion

Table 1 Species considered in the models

Feeding gas	Plasma species
$He + N_2$	e, He, N_2, He^+, He_2^+, He*, He_2*, N_2^+, N_4^+
$He + O_2$	e, He, O_2, O_2^+, O_4^+, O^-, O_2^-, O_3^-, He*, He_2*, O(^{1}D), O(^{1}S), $O_2(a^1\Delta_g)$, $O_2(b^1\sum_g^+)$, O_2(v), O, O_3

approximation is used in the model (4)

$$\frac{\partial n_i}{\partial t} + \nabla \cdot \boldsymbol{\Gamma}_i = S_i \tag{1}$$

$$\varepsilon_0 \nabla \cdot \boldsymbol{E} = \sum_i q_i n_i \tag{2}$$

$$\frac{\partial n_e \varepsilon}{\partial t} + \nabla \cdot \left(\frac{5}{3} \varepsilon \boldsymbol{\Gamma}_e - \frac{5}{3} n_e D_e \nabla \varepsilon \right) - e \boldsymbol{\Gamma}_e \cdot \boldsymbol{E} - \sum_j \Delta E_j R_j - \sum_k 3 \frac{m_e}{m_k} R_{el,k} k_B (T_e - T_k) \tag{3}$$

$$\boldsymbol{\Gamma}_i = \mathrm{sgn}(q_i) n_i \mu_i \boldsymbol{E} - D_i \nabla n_i \tag{4}$$

where n_i, $\boldsymbol{\Gamma}_i$, μ_i, D_i, q_i, S_i, and m_i are the density, flux, mobility, diffusion coefficient, charge, net gain/loss rate, and mass of species i, respectively. $\boldsymbol{E}$ is the electric field, ε is the mean electron energy, ε_0 is the vacuum permittivity, and k_B is the Boltzmann constant. R_{el} is the momentum transfer collisional rate between electrons and background gases and T is the temperature of plasma species. ΔE_j and R_j are the electron energy loss due to inelastic collision j and its corresponding reaction rate, respectively. Subscripts e, +, −, and k represent electron, positive ion, negative ion and background gas species (He, O_2 and/or N_2), respectively. The gas temperature is set to be 350 K.

Regarding fluxes to the electrodes, the following boundary conditions are used for charged species

$$\boldsymbol{\Gamma}_e \cdot \boldsymbol{n} = -\sigma \mu_e \boldsymbol{E} \cdot \boldsymbol{n} n_e + 0.25 v_{th,e} n_e - \gamma \sum_p \boldsymbol{\Gamma}_{+,p} \tag{5}$$

$$\boldsymbol{\Gamma}_+ \cdot \boldsymbol{n} = \sigma \mu_+ \boldsymbol{E} \cdot \boldsymbol{n} n_+ + 0.25 v_{th,+} n_+ \tag{6}$$

$$\boldsymbol{\Gamma}_- \cdot \boldsymbol{n} = -\sigma \mu_- \boldsymbol{E} \cdot \boldsymbol{n} n_- + 0.25 v_{th,-} n_- \tag{7}$$

where $\boldsymbol{n}$ is the normal vector pointing towards the wall, γ is the secondary emission coefficient and v_{th} is the thermal velocity. γ is set to 0.03 for positive ions and zero for other species, following the simplistic approach previously used by Shi and Kong [18]. The switching function σ takes a value of one when the drift velocity is directed towards the electrode and zero otherwise [19]

$$\sigma = \begin{cases} 1 & \mathrm{sgn}(q_i) \mu_i \boldsymbol{E} \cdot \boldsymbol{n} > 0 \\ 0 & \mathrm{sgn}(q_i) \mu_i \boldsymbol{E} \cdot \boldsymbol{n} \le 0 \end{cases} \tag{8}$$

For neutral species, the electrode losses are determined by incoming fluxes and surface reactions on the electrodes. These reactions, however, are difficult to predict and reaction rates are often unknown. We assume here that species reaching the electrodes will be adsorbed with a certain probability p_i, regardless of what reaction they may undergo [13]. Then, the boundary conditions are

$$\boldsymbol{\Gamma}_n \cdot \boldsymbol{n} = 0.25 v_{th} n_i p_i \tag{9}$$

Although the value of p_i is rarely known, it is predicted that the electrode loss is almost independent of p_i when $p_i > 0.01$, and even in that case the electrode loss has little influence on the plasma dynamics [13]. So, in this paper the p_i is set to be 0.01 for modelling study.

The electron energy flux to the electrodes is given by [20]

$$\boldsymbol{\Gamma}_\varepsilon \cdot \boldsymbol{n} = \frac{5}{3} \left(\frac{1}{4} \varepsilon n_e v_{th,e} - \varepsilon_r \gamma \sum \boldsymbol{\Gamma}_+ \cdot \boldsymbol{n} \right) \tag{10}$$

where ε_γ is the energy of secondary electron emitted from the electrodes and fixed at 5 eV [20]. The electron mobility and diffusivity are calculated as a function of mean electron energy using Bolsig+ [21], a Boltzmann solver. As to the transport coefficients for other species, please refer to our previous publications [13, 15].

The set of equations described above is solved using a time-dependent finite-element partial differential equation solver, COMSOL Multiphysics, and results have been post-processed with MATLAB.

3 Results and discussions

Fig. 1 shows the spatiotemporal distributions of electron density, electron generation rate, electron temperature and ion (including He^+, He_2^+, N_2^+ and N_4^+) density in $He + N_2$ CAPs with respect to the N_2 fraction ([N_2] for abbreviation). The white curves in the sub-figures indicate the sheath boundaries of the plasmas, which are defined by $|\nabla E| = 5$ kV/cm^2. This criterion for defining the sheath boundary will be discussed below. The sheath boundary benefits the following discussions on the plasma characteristics. For example, it helps to distinguish the α mode or γ mode of a plasma, because in α mode the electron generation rate dominates in the plasma bulk region, but in γ mode it dominates in the sheath region [18].

It can be seen from Figs. 1*a–d* that the electron density increases with the N_2 fraction, the same as reported in [6]. There are two main pathways for electron generation in $He + N_2$ CAPs: one is the electron-impact ionisation of the feeding gases (He and N_2), and the other is exciting helium first and then generating electrons by Penning ionisation and/or electron-impact ionisation of the helium metastables (He* and He_2^*).

Pathway 1:

$$e + He \rightarrow He^+ + e \tag{R1}$$

$$e + N_2 \rightarrow N_2^+ + e \tag{R2}$$

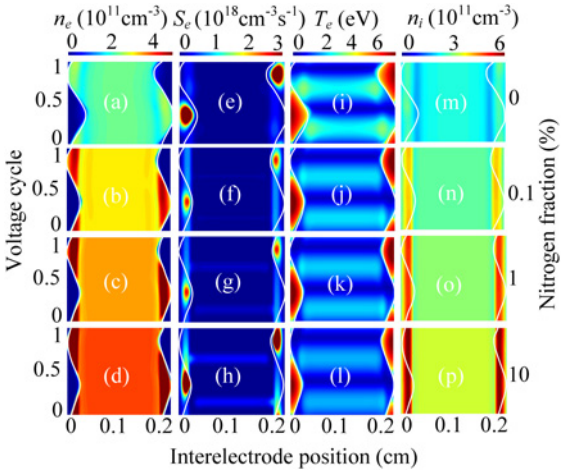

Fig. 1 *Spatiotemporal distributions of electron density, electron generation rate, electron temperature, and ion density in He + N_2 CAPs for different N_2 fractions*

High Volt., 2016, Vol. 1, Iss. 2, pp. 81–85

Pathway 2:

$$e + He \rightarrow He^* + e \quad (R3)$$

$$He^* + 2He \rightarrow He_2^* + He \quad (R4)$$

$$e + He^* \rightarrow He^+ + e \quad (R5)$$

$$He^* + N_2 \rightarrow He + N_2^+ + e \quad (R6)$$

$$He_2^* + N_2 \rightarrow 2He + N_2^+ + e \quad (R7)$$

As the increase of N_2 fraction, R1 and R5 dominate the electron production at first, and then it changes to R6 and R7, at last it transfers to R2 because the density of helium metastables decreases sharply when $[N_2] > 0.01\%$.

The electrons oscillate between the two electrodes, which has a density boundary nearly overlaps with the sheath boundary (see Figs. 1*a–d*). Although the electrons mainly exist in the plasma bulk, their generation is dominated in the sheath region regardless of the N_2 fraction (see Figs. 1*e–h*), suggesting that the plasmas keep in γ mode. This is because the electron energies needed for ionisation of helium and nitrogen in pathway 1 and an excitation of helium in pathway 2 are high, at least 15.4 eV for the ionisation of nitrogen (R2), and consequently the electrons in the sheath region are most involved in the two pathways for electron generation. The average electron energy in sheath region is much larger than that in the bulk region according to the electron temperature distribution as shown in Figs. 1*i–l*.

The ion density increases with the N_2 fraction as shown in Figs. 1*m–p*. This is in accordance with the trend of electron density because of the electropositive and quasi-neutral nature of the $He + N_2$ CAPs, i.e. the electron density roughly equals to the ion density. The ion densities peak at the interface of the bulk and sheath regions, because the ions are mainly generated in the sheath and they stay there almost regardless of the oscillation of the sheath boundary. The distribution of ions keeps invariable with time, much different to that of electrons, because the ion mobilities are typically less than the electron mobility by ~50 folds [22].

Compared to the electropositive CAPs in $He + N_2$ mixtures, the plasma characteristics of $He + O_2$ CAPs are much different due to their electronegative nature, as shown in Fig. 2. Some sub-figures in Fig. 2 are similar to our previous reports in [4], but the sheath boundary curves are different due to the change in the criterion. The sub-figures are plotted here to facilitate the comparison between $He + O_2$ and $He + N_2$ CAPs.

As shown in Figs. 2*a–d*, the electron density decreases with the increasing O_2 fraction, because many electrons are loosed via the electron attachment reactions as follows

$$e + O_2 \rightarrow O + O^- \quad (R8)$$

$$e + O_2 + He \rightarrow He + O_2^- \quad (R9)$$

Many anions are generated via R8 and R9, and hence the electronegativity (n_-/n_e) increases from 0 to 123 with the O_2 fraction from 0 to 10%. The plasma becomes to have typical electronegative feature when $n_-/n_e > 1$, corresponding to $[O_2] > 0.2\%$ in $He + O_2$ CAPs. The electron distribution changes greatly, in particular, the density boundary of electrons no longer overlaps with the sheath boundary when $[O_2] \geq 1\%$ (see Figs. 2*c* and *d*). The electron generation rate dominates in the sheath region when $[O_2] \leq 0.1\%$, but it dominates in the bulk region when $[O_2] \geq 1\%$ (see Figs. 2*e–h*), indicating that the discharge transfers from γ mode to α mode as it changes from an electropositive plasma to an electronegative one. The electron temperature decreases in the sheath region, but increases in the bulk region with increasing O_2 fraction (see Figs. 2*i–l*), leading to similar trends of ionisation and excitation rate coefficients of helium (R1 and R3) in both regions, and therefore it is an important reason for the γ to α mode transition. The distributions of ions (including O_2^+, O_4^+, O^-, O_2^-, and O_3^-) are much different to that of the electropositive plasmas, especially for the ion density peaking at the centre position of the discharge gap (see Figs. 2*n–p*) rather than at the bulk-sheath interface (see Figs. 1*n–p*). This is mainly because the anions are confined in the bulk region by the ambipolar electric field. The ion density first increases and then decreases with the increasing O_2 fraction, but the electronegativity keeps increasing due to the continuous drop of electron density.

The spatial distributions of the half-cycle averaged electric fields are shown in Figs. 3*a* and *b* for $He + N_2$ and $He + O_2$ CAPs, respectively. Each curve corresponds to an impurity (N_2 or O_2) fraction of 0, 0.1, 1, or 10%. It can be seen that the spatial distribution of the averaged electric field in $He + N_2$ discharge is relatively independent of the impurity fraction. In contrast, in $He + O_2$ discharge it decreases in the sheath region and increases in the bulk region as the increasing impurity fraction. The dependence of the electric field on the impurity fraction is similar to that of the electron temperature either for the electropositive or the electronegative CAPs, as shown in Figs. 1 and 2.

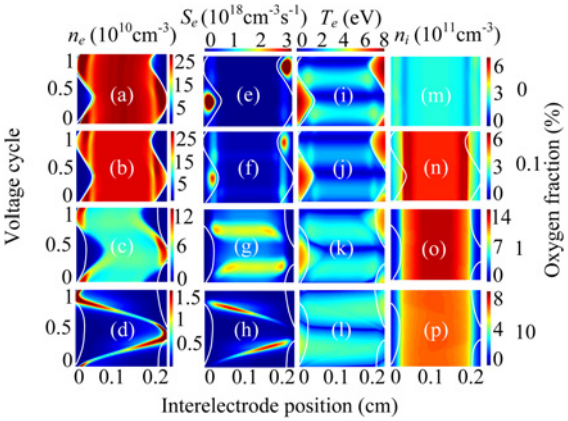

Fig. 2 *Spatiotemporal distributions of electron density, electron generation rate, electron temperature, and ion density in He + O_2 CAPs for different O_2 fractions*

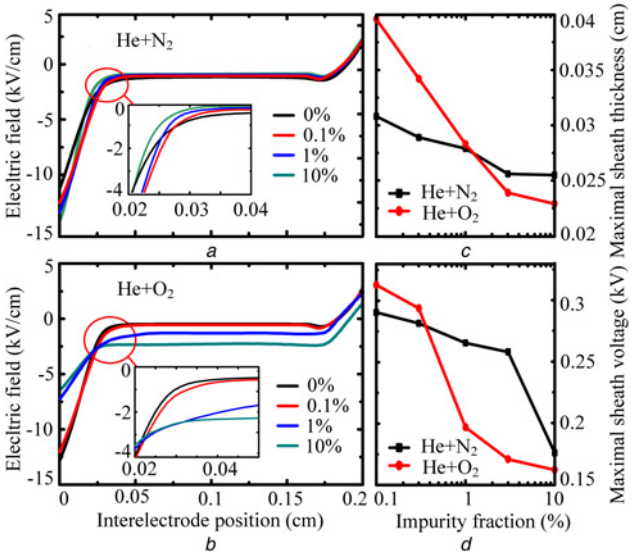

Fig. 3 *Half-cycle averaged profiles of the electric fields and the sheath characteristics in He + N_2 and He + O_2 plasmas*

a Spatial distribution of electric field in $He + N_2$
b Spatial distribution of electric field in $He + O_2$
c, *d* max width and max voltage of the plasma sheaths in $He + N_2$ and $He + O_2$

Determining the boundary of plasma sheath is very important for characterising a plasma, for which several criteria have been reported, such as 14% of the maximal electric field [23], $E = 1$ kV/cm [24], and $n_e = 0.3(n_+ - n_-)$ [4]. These criteria are suitable for electropositive CAPs, but maybe not for electronegative CAPs as reported here. For example, when the O_2 fraction is 10% the averaged electric field in the plasma bulk is ~2.5 kV/cm, more than one-third of the maximal electric field (see Fig. 3*b*). One typical feature of CAPs is that the electric field varies little in the bulk region, but keeps rising or dropping from the bulk-sheath interface to the electrode surface, as shown in Figs. 3*a* and *b*. This suggests that the gradient of the electric field can be used as a criterion for determining the sheath boundary. In this paper, the absolute value of such gradient, $|\nabla E| = 5\,\mathrm{kV/cm^2}$, is chosen as the criterion, which is capable of capturing the turning point of each electric field curve (see the inset images in Figs. 3*a* and *b*), and hence suitable for both the electropositive and electronegative CAPs.

Based on the sheath boundary criterion, it is found that the sheath thicknesses of both $He + N_2$ and $He + O_2$ CAPs decrease with the increasing impurity concentration, but for $He + O_2$ CAPs the decrement is larger (see Fig. 3*c*). This trend also applies for the voltage drops in the sheaths as shown in Fig. 3*d*. As the increase of oxygen fraction in $He + O_2$ CAPs, the decrease of electron density in the bulk region (see Figs. 2*a–d*) leads to the increase of plasma resistance, while the decrease of voltage drop across the sheath region indicates the decrease of plasma capacitance, and therefore the electrical feature of the discharge transforms from capacitive to resistive as it changes from electropositive to electronegative. A similar difference of electrical feature has been reported for low-pressure argon (electropositive) and SF_6 (electronegative) plasmas [25].

In low-pressure plasmas, the total current in the bulk region is carried mostly by electrons [25, 26]. This is mainly because the electron mobility is larger than that of ions by ~50 folds, and the electron density is comparable to the ion density. This situation is changed in atmospheric-pressure plasmas, because most voltage drops in the sheath where the ion density is much larger than the electron density, so much energy is coupled to the ions which may not be ignored. In particular, CAPs are much easier to be electronegative compared to their low-pressure counterparts due to the frequency collisions between electrons and the working gases, and in that case the ion density may be much larger than the electron density, resulting in even larger portion of the discharge energy coupled to the ions. In order to elucidate the energy dissipation characteristics in different kinds of CAPs, we plot in Fig. 4 the spatiotemporal distributions of electron- and ion-coupling power densities for $He + N_2$ and $He + O_2$ CAPs, with respect to the impurity fractions of 0, 0.01, 0.1, 1, and 10%. P_e and P_i are the numerical results for electron-coupling power density and ion-coupling power density, respectively.

For $He + N_2$ CAPs, most of the input power is coupled to the electrons, but in the sheath a unnegligible portion of the input power is coupled to the ions (see Fig. 4). This is in accordance to the $He + O_2$ CAPs when the oxygen fraction is low (electronegativity < 1). However, when the electronegativity is high, much more power will be coupled to the ions, and even when $[O_2] = 10\%$ the ion-coupling power dominates.

The spatiotemporal averaged power dissipations on electrons and ions in $He + N_2$ and $He + O_2$ CAPs are shown in Fig. 5, as a function of the impurity fraction from 0.01 to 10%. Besides the numerical results (P_e and P_i) of solid curves, two dash curves namely $P_{e,ohm}$ and $P_{i,es}$ are also plotted in Fig. 5 for the purpose of theoretical analysis. $P_{e,ohm}$ represents the power dissipated for ohmic heating of electrons, which can be calculated as follows [27]

$$S_{ohm} = \frac{0.5 m_e \nu_m l_B}{n_e} \Gamma_e^2 \tag{11}$$

where ν_m is electron neutral collision frequency (~$10^{12}\,\mathrm{s^{-1}}$ at atmospheric pressure) and l_B is the plasma bulk length. $P_{i,es}$

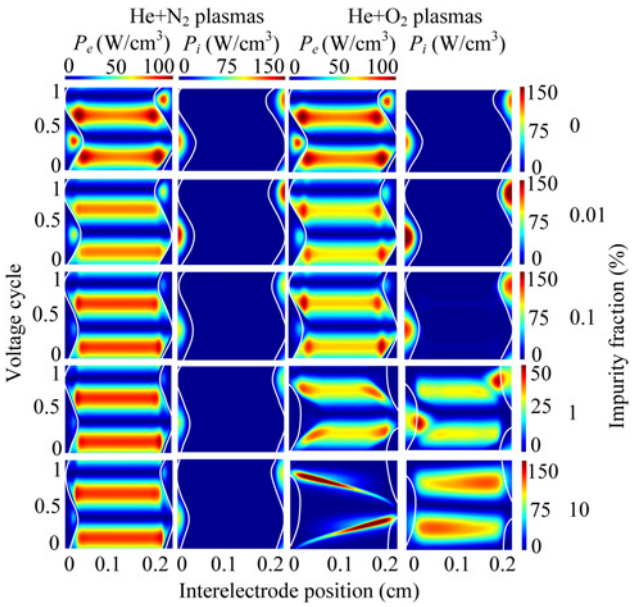

Fig. 4 *Spatiotemporal distributions of power dissipation on electrons and ions in He + N_2 and He + O_2 CAPs*

represents the power dissipation on the ions that estimated according to their densities and mobilities. In the bulk regions of plasmas, the electrons and ions are assumed to have densities invariable with the electrode gap position, and therefore their density relationship can be roughly estimated by the neutralisation feature of the plasmas, as given by

$$(n_+ + n_e)/n_e = 2\xi + 1 \tag{12}$$

where ξ represents the electronegativity. Assuming the ions have the same mobility of $\mu_{ion} = 20\ \mathrm{cm^2/s}$, while for electrons it is $1056\ \mathrm{cm^2/s}$ [28]. The ion-coupling power density in the bulk region can be calculated as follows

$$P_{ion,b} = \frac{\mu_{ion}(2\xi + 1)}{\mu_e n_e + \mu_{ion}(2\xi + 1)} P_{in} \tag{13}$$

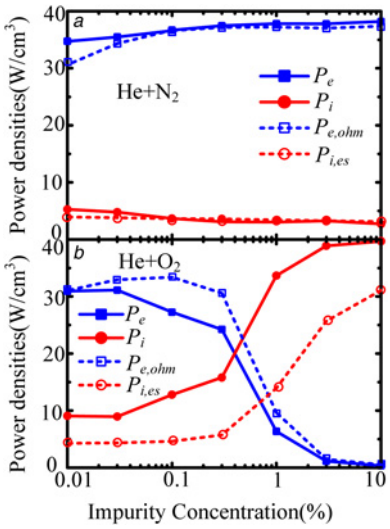

Fig. 5 *Spatiotemporal averaged profiles of power dissipations on electrons and ions in He + N_2 and He + O_2 CAPs as a function of impurity fraction*

a $He + N_2$
b $He + O_2$

High Volt., 2016, Vol. 1, Iss. 2, pp. 81–85

where $P_{\mathrm{ion,b}}$ represents the ion-coupling power density in the bulk region and P_{in} the input power density which is assumed invariable with the locations.

In the sheath region, the relationship of ion density and electron density cannot be roughly estimated by the electronegativity. However, the ion current should equal to the electron current due to the quasi-neutral nature of the plasmas, and hence the ion-coupling power can be roughly estimated the same as the electron-coupling power in the sheath. For the entire plasma, the spatiotemporal averaged power coupled by ions can be given by

$$P_{i,\mathrm{es}} = P_{\mathrm{in}}\left(\frac{\mu_{\mathrm{ion}}(2\xi+1)}{\mu_{\mathrm{e}}+\mu_{\mathrm{ion}}(2\xi+1)}l_{\mathrm{b}}+\frac{l_{\mathrm{s}}}{2}\right)\Big/ l \tag{14}$$

where l_{s} is the sheath thickness and l is the total gap between electrodes.

It can be seen from Fig. 5 that about 90% of the input power is coupled to the electrons in $He + N_2$ CAPs, relatively independent of the N_2 fraction. On contrast, the electron-coupling power decreases with the increasing O_2 concentration in $He + O_2$ CAPs, in particular, it is smaller than the ion-coupling power when $[O_2]$ ~0.5%. The calculated results of electron-coupling power densities are similar to the numerical ones, suggesting that the ohmic heating is the main electron heating mechanism. Moreover, the calculated results of ion-coupling power densities agree well with the numerical ones for $He + N_2$ CAPs, and they are a little smaller, but with a similar trend to the numerical results for $He + O_2$ CAPs. Therefore, formulas (11) and (14) for calculating the electron- and ion-coupling powers are reliable, which can be used for estimating the power dissipation characteristics of CAPs.

4 Concluding remarks

In this paper, $He + N_2$ and $He + O_2$ CAPs are chosen as the representatives for electropositive and electronegative plasmas, of which the discharge characteristics are studied and then compared to each other by fluid models. As the increase of the impurity (N_2 or O_2) fraction, for $He + N_2$ CAPs the electron density and ion density increase, the spatiotemporal distributions of electron density, ion density, electron temperature, and electron generation rate change a little, e.g. the ion density has two peaks at the bulk-sheath interface, and the electron generation rate dominates in the sheath which indicates that the plasmas are kept in γ mode. On contrast, for $He + O_2$ CAPs the electron density decreases, the ion density first increases and then decreases, the electron temperature increases in the bulk region, but decreases in the sheath region, and the plasmas transform from γ mode to α mode as the distribution of electron generation rate changes a lot.

The $He + N_2$ CAPs are capacitive in nature, but the $He + O_2$ CAPs becomes more and more resistive as the increase of O_2 fraction. This is because the electron density in the bulk region decreases sharply and hence larger electric field is needed to sustain the plasmas. The increase of electric field in the bulk region makes the sheath boundary more difficult to be determined, and several criteria reported in the literature are found to be not applicable. A new criterion of the sheath boundary, $|\nabla E| = 5\,\mathrm{kV/cm^2}$, is put forward, which is found suitable for both the electropositive and electronegative CAPs.

Most of the input power is dissipated into electrons in $He + N_2$ CAPs via ohmic heating, but for $He + O_2$ CAPs more and more input power is coupled to ions with increasing O_2 fraction. The ion-coupling power even dominates when $[O_2] > 0.5\%$. A formula is put forward to estimate the ion-coupling power, of which the calculated results are similar to the numerical ones.

5 Acknowledgment

This work was supported by the National Science Foundation of China (Grant No. 51521065), the Fundamental Research Funds for the Central Universities and the State Key Laboratory of Electrical Insulation and Power Equipment (Grant No. EIPE14123).

6 References

1 Malik, M.A., Ghaffar, A., Malik, S.A.: 'Water purification', *Plasma Sources Sci. Technol.*, 2001, **10**, (1), pp. 82–91
2 Kong, M.G., Kroesen, G., Morfill, G., *et al.*: 'Plasma medicine: an introductory review', *New J. Phys.*, 2009, **11**, (11), p. 115012
3 Mariotti, D., Patel, J., Švrček, V., *et al.*: 'Plasma-liquid interactions at atmospheric pressure for nanomaterials synthesis and surface engineering', *Plasma Processes Polym.*, 2012, **11**, (9), pp. 1074–1085
4 Yang, A.J., Liu, D.X., Rong, M.Z., *et al.*: 'A dominant role of oxygen additive on cold atmospheric-pressure $He + O_2$ plasmas', *Phys. Plasmas*, 2014, **21**, (8), p. 083501
5 Park, J., Henins, I., Herrmann, H.W., *et al.*: 'An atmospheric pressure plasma source', *Appl. Phys. Lett.*, 2000, **76**, (3), pp. 288–290
6 Martens, T., Bogaerts, A., Brok, W.J.M., *et al.*: 'The dominant role of impurities in the composition of high pressure noble gas plasmas', *Appl. Phys. Lett.*, 2008, **92**, (4), p. 041504
7 Yuan, X.H., Raja, L.L.: 'Role of trace impurities in large-volume noble gas atmospheric-pressure glow discharges', *Appl. Phys. Lett.*, 2002, **81**, (5), pp. 814–816
8 Liu, D.X., Bruggeman, P., Iza, F., *et al.*: 'Global model of low-temperature atmospheric-pressure $He + H_2O$ plasmas', *Plasma Sources Sci. Technol.*, 2010, **19**, (2), p. 025018
9 Liu, D.X., Wang, X.H., Rong, M.Z., *et al.*: 'Main species and physicochemical processes in cold atmospheric-pressure $He + O_2$ plasmas', *Plasma Processes Polym.*, 2010, **9**, (7), pp. 846–865
10 Schmidt-Bleker, A., Winter, J., Iseni, S., *et al.*: 'Reactive species output of a plasma jet with a shielding gas device-combination of FTIR absorption spectroscopy and gas phase modeling', *J. Phys. D, Appl. Phys.*, 2014, **47**, (14), p. 145201
11 Kanazawa, S., Kogoma, M., Moriwaki, T., *et al.*: 'Stable glow plasma at atmospheric pressure', *J. Phys. D, Appl. Phys.*, 1988, **21**, (5), pp. 838–840
12 Liu, D.X., Yang, A.J., Wang, X.H., *et al.*: 'Wall fluxes of reactive oxygen species of an rf atmospheric-pressure plasma and their dependence on sheath dynamics', *J. Phys. D, Appl. Phys.*, 2012, **45**, (30), p. 305205
13 Yang, A.J., Wang, X.H., Rong, M.Z., *et al.*: '1-D fluid model of atmospheric-pressure rf $He + O_2$ cold plasmas: Parametric study and critical evaluation', *Phys. Plasmas*, 2011, **18**, (11), p. 113503
14 Wang, X.H., Yang, A.J., Bai, C.F., *et al.*: 'Time difference between the density peaks of species and current peak in dielectric barrier discharge', *High Voltage Eng.*, 2012, **38**, (supplement), pp. 546–549
15 Yang, A.J., Wang, X.H., Liu, D.X., *et al.*: 'Temporal modulation of plasma species in dielectric barrier discharges', *Phys. Plasmas*, 2014, **21**, (7), p. 073507
16 Yang, A.J., Wang, X.H., Rong, M.Z., *et al.*: 'The influence of impurities on mode transition in atmospheric-pressure electronegative plasmas', *High Voltage Eng.*, 2012, **38**, (supplement), pp. 574–577
17 Liu, D.W., Iza, F., Kong, M.G.: 'Evolution of atmospheric-pressure RF plasmas as the excitation frequency increases', *Plasma Processes Polym.*, 2009, **6**, (6), pp. 446–450
18 Shi, J.J., Kong, M.G.: 'Mechanisms of the α and γ modes in radio-frequency atmospheric glow discharges', *J. Appl. Phys.*, 2005, **97**, (2), p. 023306
19 Hagelaar, G.J..M., de Hong, F.J., Kroesen, G.M.W.: 'Boundary conditions in fluid models of gas discharges', *Phys. Rev. E*, 2000, **62**, (1), pp. 1452–1454
20 Sakiyama, Y., Graves, D.B.: 'Nonthermal atmospheric rf plasma in one-dimensional spherical coordinates: asymmetric sheath structure and the discharge mechanism', *J. Appl. Phys.*, 2007, **101**, (7), p. 073306
21 Hagelaar, G.J.M., Pitchford, L.C.: 'Solving the Boltzmann equation to obtain electron transport coefficients and rate coefficients for fluid models', *Plasma Sources Sci. Technol.*, 2005, **14**, (4), pp. 722–733
22 Lindinger, W., Albritton, D.L.: 'Mobilities of various mass-identified positive ions in helium and argon', *J. Chem. Phys.*, 1975, **62**, (9), pp. 3517–3522
23 Shi, J.J., Kong, M.G.: 'Cathode fall characteristics in a dc atmospheric pressure glow discharge', *J. Appl. Phys.*, 2003, **94**, (9), pp. 5504–5513
24 Shi, J.J., Kong, M.G.: 'Mode characteristics pf radio-frequency atmospheric glow discharges', *IEEE Trans. Plasma Sci.*, 2005, **33**, (2), pp. 624–630
25 Gogolides, E., Sawin, H.H.: 'Continuum modeling of radio-frequency glow discharges. I. Theory and results for electropositive and electronegative gases', *J. Appl. Phys.*, 1992, **72**, (9), pp. 3971–3987
26 Monahan, D.D., Turner, M.M.: 'Global models of electronegative discharges: critical evaluation and practical recommendations', *Plasma Sources Sci. Technol.*, 2008, **17**, (4), p. 045003
27 Lieberman, M.A., Lichtenberg, A.J.: 'Principles of Plasma Discharges and Materials Processing'. New York, 2005
28 Wang, Q., Economou, D.J., Donnelly, V.M.: 'Simulation of a direct current microplasma discharge in helium at atmospheric pressure', *J. Appl. Phys.*, 2006, **100**, (2), p. 023301